

<https://doi.org/10.1038/s42004-025-01880-w>

# Probing non-radiative quantum relaxation in fluorophores using an optical fiber Bragg grating photothermal sensor

Check for updates

Sweta Rath<sup>1,2,3</sup>, Sagi Shiva Sreenivasa Dheerendra Koushik<sup>1,2,3</sup> & Shivananju Bannur Nanjunda <sup>1,2,3</sup>

While optical fiber Bragg gratings (FBGs) have been exploited in the field of sensing, their potential for investigating quantum processes of photon-molecule interactions remains unexplored. Here, we experimentally demonstrated a method of probing photon-induced non-radiative thermal relaxation in fluorophores using the FBG technique. In response to various excitation wavelengths of photons, the FBG with fluorescent dye, Rhodamine B, present on its cladding, exhibits distinct Bragg wavelength shifts, reflecting the level of vibronic transitions and the absorption characteristics of the fluorophore based on non-radiative thermal release. The photoexcitation intensity-dependent response demonstrates that the FBG technique can probe localized photothermal relaxation at the micron-scale with LED intensity below  $5 \text{ mW cm}^{-2}$ . Moreover, the modulation of the observed split in the Bragg wavelength spectrum provides further insights into photothermal localization in addition to yielding photothermal information. This approach of realizing photon-molecule interaction makes fiber Bragg grating-based quantum phenomena sensing accessible and can be extended for spectroscopy, biosensing, and quantum applications.

The discovery of photosensitivity in optical fibers led to the emergence of fiber Bragg grating (FBG) technology, characterized by a periodic modulation of the refractive index inscribed within the core of the optical fiber. These act as wavelength-selective grating planes, reflecting a specific narrow band of wavelengths, with the peak reflection known as the Bragg wavelength ( $\lambda_B$ ), determined by the parameters defined in Eq. 1<sup>1</sup>.

$$\lambda_B = 2n_{\text{eff}}\Lambda \quad (1)$$

where  $\Lambda$  denotes the grating pitch, and  $n_{\text{eff}}$  represents the effective refractive index of the FBG resulting from the indices of refraction of grating, core, and cladding. While early research primarily focused on the fabrication process of FBG, subsequent research shifted attention to its diverse applications, leading to successful commercial implementation in the telecommunication industry, structural health monitoring, and the medical field<sup>1-4</sup>. In the recent decade, scientists have exploited FBGs for studying photon-matter interactions in nanomaterials, including carbon nanotubes (CNTs), chalcogenides, and two-dimensional materials<sup>5-12</sup>. Here, photo-induced strain or photothermal effect in nanomaterials is probed by the change in the

reflected Bragg wavelength as described by the following expression<sup>1</sup>.

$$\Delta\lambda_B = 2\left(\Lambda \frac{\partial n_{\text{eff}}}{\partial T} + n_{\text{eff}} \frac{\partial \Lambda}{\partial T}\right)\Delta T + 2\left(\Lambda \frac{\partial n_{\text{eff}}}{\partial l} + n_{\text{eff}} \frac{\partial \Lambda}{\partial l}\right)\Delta l \quad (2)$$

The first term in Eq. 2 denotes the variation in the effective refractive index and the grating pitch due to photoinduced temperature changes, while the second term represents alterations in these parameters due to photoinduced strain. Despite these studies on FBG-based photon-matter interaction, which have focused on detecting transient changes in material properties owing to photon absorption, there has not been any report on probing photon-induced non-radiative thermal relaxation process, especially in fluorescent molecules using the FBG technique.

Photoluminescence or molecular fluorescence is the optical emission from molecules excited to higher energy levels by absorbing appropriate photon energy. The emitted photons have a higher wavelength, resulting in lesser photon energy than absorbed photons due to non-radiative transitions, such as vibrational relaxations in the excited levels, during which the absorbed photon energy is released as heat<sup>13</sup>. Experimental determination of non-

<sup>1</sup>Department of Electrical Engineering, Indian Institute of Technology Madras, Chennai, India. <sup>2</sup>Centre of Excellence in Biochemical Sensing and Imaging Technologies (Cen-Bio-Sim), Indian Institute of Technology Madras, Chennai, India. <sup>3</sup>Institute of Excellence in Healthcare and Assistive Technologies, Indian Institute of Technology Madras, Chennai, India. ✉ e-mail: [shivananju@ee.iitm.ac.in](mailto:shivananju@ee.iitm.ac.in)

radiative photothermal dissipation is important for molecular characterization, for developing fluorophores with optimal photothermal conversion, which can benefit the medical field, facilitating simultaneous photothermal therapy and imaging, and for improving biosensing applications.

Conventional photothermal measurement methods, including thermometers and infrared (IR) cameras, are restricted to assessing macroscopic temperatures with low temporal and spatial resolution. Consequently, the thermal information recorded by these techniques may be significantly lower than the actual localized heat generated during photon-molecule interactions<sup>14</sup>. While thermometers are mainly applicable to liquid samples, thermal IR cameras are prone to ambient atmospheric temperature, thermal emissivity of the sample surface, and the measured distance from the sample, which lowers their accuracy<sup>15,16</sup>. Moreover, thermometers, thermocouples, and thermistors or RTDs are susceptible to self-heating due to the absorption of incident photons, making them unsuitable for accurately measuring photothermal effects<sup>16–19</sup>.

Advancements in nano-thermometry have introduced innovative techniques for measuring temperature at the nanoscale, offering alternatives to traditional thermometry methods<sup>20–22</sup>. Nano-thermometry methods, such as scanning thermal microscopy (SThM)/ atomic force microscopy (AFM) using a microthermocouple probe or a cantilever probe integrated with microscopy imaging<sup>23–27</sup>, deliver exceptional thermal and spatial resolution but are limited to surface temperature measurements of the sample. Additionally, these techniques require complex experimental setups and intricate data analysis, often necessitating scanning microscopy, which restricts the range of samples that can be examined<sup>20</sup>. Also, for photothermal studies, careful design consideration is required for sample placement to shield the probe tip from direct light exposure, which otherwise can falsify the temperature readings<sup>25,26</sup>.

Thermal mapping techniques, such as interferometry-based optical microscopy<sup>28,29</sup> and Raman spectroscopy<sup>30–32</sup>, can provide internal thermal information from a sample. However, Interferometry relies on uniform illumination (Köhler illumination) along with additional optics for even excitation at the sample surface, and a wavefront analyzer, making the retrieval of photothermal information more complex. Raman spectroscopy, while capable of extracting photothermal information across diverse samples, needs the sample to exhibit thermally sensitive Raman-active phonon modes and requires a high-resolution spectrometer and/or strong excitation power to capture the weak Raman signal. Additionally, this technique encounters challenges when applied to fluorescent samples, as their high emission intensity can overshadow the weak Raman peaks<sup>20</sup>.

So far, the techniques mentioned above have predominantly been used for photothermal detection in plasmonic nanostructures, utilizing near-infrared or infrared light as the excitation source, with very few attempts made to probe the non-radiative heat generated in fluorescent molecules when exposed to visible photons<sup>27</sup>.

Over the past few decades, several popular non-destructive and highly sensitive thermo-optical techniques have been proposed for photothermal study of various samples, including fluorescent materials<sup>18,33–39</sup>. Key techniques include thermal lens spectroscopy or microscopy, photothermal deflection and displacement spectroscopy, photoacoustic spectroscopy, and photothermal interferometry. While thermal lens and photothermal deflection/displacement spectroscopy rely on probe beam deflection due to changes in the medium's refractive index, the effectiveness of these techniques is influenced by factors such as high-intensity, stabilized laser radiation, the medium's thermo-optic coefficient, and the probe beam wavelength. These techniques require complex mathematical modeling for retrieving thermal information and are sensitive to the geometrical parameters of the optical setup, necessitating careful calibration. Photoacoustic spectroscopy measures pressure wave changes from non-radiative thermal expansion, but is affected by stray signal interference. Photothermal interferometry detects phase changes in the probe beam due to refractive index modulation, offering high sensitivity but necessitating complex Michelson or Mach-Zehnder interferometry setups that are sensitive to environmental factors and need precise adjustments<sup>34</sup>.

To address these limitations, this work presents an approach to capturing the non-radiative thermal relaxation of photon-molecule interactions, particularly in fluorophores, using a highly sensitive FBG technique, where the measurements are wavelength-encoded. Although various spectrally encoded thermometry techniques, such as those utilizing lanthanide-based or up-conversion nanoparticles (UCNPs)<sup>40,41</sup> and nanodiamonds (NV centers)<sup>42,43</sup> have been reported for high-resolution thermal mapping, these techniques fundamentally differ from the Bragg wavelength spectral encoding approach for photothermal information discussed in this work. The merits of FBG-based photothermometry lie in its simple experimental setup, immunity to external electromagnetic interference, absence of photon-induced self-heating with visible excitation, chemical inertness, and flexibility in choosing the excitation wavelength. Here, we demonstrate that Bragg wavelength shifts recorded from FBG during photoexcitation of a common fluorescent molecule, Rhodamine B (RhB), can give insight into the molecular vibronic transition levels as well as its absorption characteristics based on the non-radiative thermal release during photon-molecule interaction. The excitation photon intensity-dependent Bragg wavelength response demonstrates the high linearity of the sensor, enabling photothermal characterization at a low excitation intensity of a few mW cm<sup>-2</sup>. Further, we demonstrate a method of capturing the photothermal information and thermal localization based on Bragg spectral split modulation originating from non-uniform illumination of the fluorescent sample. Further, a comparison between FBG and the conventional IR camera shows highly sensitive detection of localized non-radiative photothermal relaxation at the micron-scale with the proposed approach.

## Results and discussion

### Experimental setup

The schematic, as well as the actual experimental setup used for demonstrating non-radiative photothermal detection in fluorophores with FBG, are shown in Fig. 1a and b, respectively. The setup comprises an inverted fluorescence microscope (Olympus IX83) containing a broadband LED light source with various wavelength filters to photoexcite the fluorescent dye-coated FBG externally at specific optical narrow-band wavelengths while capturing the fluorescence phenomena with the equipped camera, and an FBG interrogator for measuring the Bragg wavelength shift resulting from the interaction between the excitation photons and the fluorophores. The RhB-coated FBG sensor affixed to a glass substrate was kept on the movable stage of the inverted fluorescence microscope, and its position was adjusted by XY piezo controller such that the region encompassing the FBG was exposed to the light beam from the microscope perpendicular to the fiber axis. A continuous beam of white light from the LED source, after being filtered through the excitation wavelength filter and reflected from the dichroic mirror, transversely illuminated the RhB-FBG sensor through the microscope objective lens. The emitted fluorescence beam passing through the same objective lens and dichroic beam splitter was filtered by the emission filter and detected by a highly sensitive camera (ORCA-Flash 4.0 V3 sCMOS camera). Concurrently, a broadband light (1510–1590 nm) was launched into the core of the RhB-coated FBG, and the change in the Bragg wavelength arising from photon-molecule interaction was measured with an optical FBG interrogator connected to one end of the fiber.

### Preparation of Rhodamine B-coated FBG and characterization study

Optical fiber Bragg grating was fabricated on a photosensitive germania-doped silica single-mode fiber (SMF, 4.2/125 μm) having a 4.2 μm diameter core with a refractive index of 1.47, and a 125 μm diameter cladding with a refractive index of 1.44. Phase mask technique was used to inscribe a 3 mm grating inside the fiber core, which provides a central Bragg wavelength of around 1560 nm. Rhodamine B was coated on the grating region of FBG on top of its cladding by following previously reported coating procedures<sup>44,45</sup>

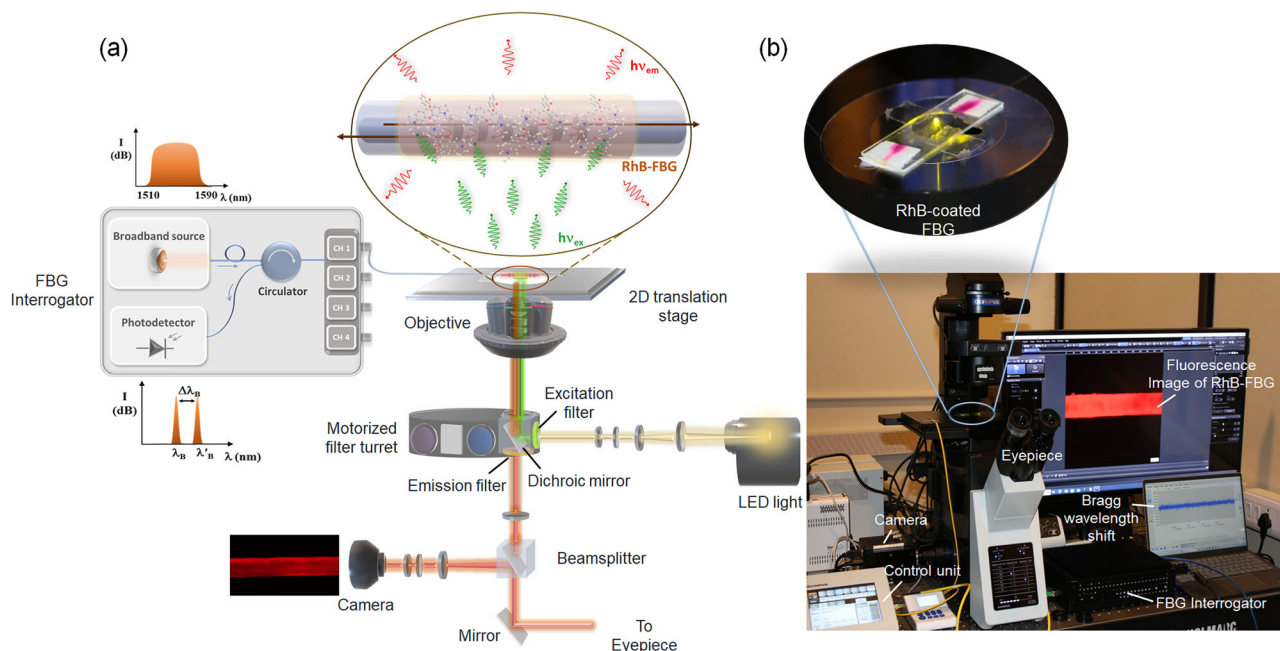


**Fig. 1 | Experimental demonstration for probing non-radiative photothermal relaxation in fluorescent molecules with FBG.** **a** Experimental layout and **b** real-time experimental setup for demonstrating non-radiative photothermal detection in

fluorophores with FBG. Shown is an epi-illumination inverted fluorescence microscope with a glass slide containing RhB-FBG on top and an optical FBG interrogator connected to RhB-FBG on the side.

with slight modification (refer to methods section), which involves suitable functionalization of the fiber surface followed by a simple drop-casting technique as portrayed in Fig. 2a.

The morphology, chemical composition, and thickness of the Rhodamine B coating on FBG were investigated using various characterization techniques. The Scanning Electron Microscopy (SEM) image (Fig. 2b) shows the intact coating of rhodamine molecules around the cylindrical FBG surface. Inset is the enlarged SEM view showing the morphology of RhB particles in the form of pellet-like shapes, and these are observed to form clusters over the fiber surface. The Raman spectrum obtained from the RhB-coated FBG surface at 633 nm excitation wavelength is shown in the Supplementary Fig. 1. The spectrum (Fig. 2c) resulting from background subtraction due to fluorescence depicts typical Raman peaks of silica fiber at 440, 486, and 800  $\text{cm}^{-1}$ <sup>46</sup> and for Rhodamine B at characteristic wavenumbers dominated by xanthene ring vibration (622  $\text{cm}^{-1}$ ), C–H in-plane bend vibration (1200  $\text{cm}^{-1}$ ), C–C bridge band stretch vibration (1281  $\text{cm}^{-1}$ ), and aromatic stretch vibrations (1359, 1534, and 1650  $\text{cm}^{-1}$ )<sup>47,48</sup>. The Atomic Force Microscopy (AFM) image (Fig. 2d) clearly shows the thickness of the rhodamine coating around 650 nm. Finally, the Energy-Dispersive X-ray Spectroscopy (EDX) spectroscopy result (Fig. 2e) shows the elemental composition of the coating material. The reflection and transmission spectra of FBG taken before and after RhB coating (Supplementary Fig. 2) indicate no significant changes in the spectrum following the RhB coating.

### Detection of non-radiative photothermal relaxation with FBG

**Theoretical background.** Fluorescent organic dye Rhodamine B, known for its excellent quantum efficiency<sup>49</sup>, broad wavelength absorption<sup>39</sup>, and strong thermal<sup>50</sup> and photo-stability<sup>51</sup>, is composed of a three-ring xanthene chromophore, primarily responsible for photon energy absorption and emission<sup>52</sup>, and a benzene ring with a carboxyl group oriented perpendicular to the plane of the xanthene. The UV-visible absorption and fluorescence spectra of RhB dye dissolved in water (Fig. 3a) exhibit excitation and emission bands with peaks at 554 nm and 584 nm, respectively, where the characteristic absorption peaks are attributed to  $\pi-\pi^*$  electronic transitions between bonding and anti-bonding molecular orbitals<sup>53</sup>. Figure 3b illustrates the typical electronic

transitions in rhodamine molecules that govern absorption and emission spectra. The primary absorption band in the visible region (450–600 nm), known as the Q-band, is assigned to the  $S_0-S_1$  transition, while the Soret band in the near-UV region (350–400 nm) is attributed to the  $S_0-S_2$  transition<sup>53,54</sup>. These electronic transitions are often coupled with vibrations of different frequencies represented as dashed lines in Fig. 3b.

**Principle.** Photoexcitation of RhB molecules deposited on FBG with energies corresponding to its absorption band causes electrons to transit from ground state  $S_0$  to various vibrational levels of excited singlet states ( $S_1$  and  $S_2$ ) (Fig. 3b). After rapid relaxation to a thermally equilibrated excited state by releasing excess absorbed photon energy non-radiatively as heat through internal conversion (induced by molecular vibrations) and vibrational relaxation, electrons return to the ground state, radiatively releasing the remaining absorbed energy as longer-wavelength photons<sup>13,55</sup>. However, due to the aggregation of rhodamine molecules or the formation of dimers in the thin-film coating<sup>56,57</sup>, there is also a high probability of non-radiative energy transfer<sup>58,59</sup> (a de-excitation pathway<sup>60</sup>) induced by coupling to the lattice vibrations or phonons<sup>59–61</sup>. These photo-excitations, accompanied by electron redistribution and vibronic transitions in rhodamine molecules<sup>62</sup>, followed by non-radiative thermal dissipation of absorbed photon energy<sup>13,61</sup>, can impact the FBG grating parameters such as the effective refractive index and the grating periodicity, consequently leading to a shift in the Bragg wavelength as represented by the following expression (Eq. 3)<sup>9</sup>.

$$\Delta\lambda_B = 2 \left( \Lambda \frac{\partial n_{\text{eff}}}{\partial T} + n_{\text{eff}} \frac{\partial \Lambda}{\partial T} \right) (\Delta T_{\text{non-radiative relaxation}}) \quad (3)$$

Equation 3 describes the photon-induced non-radiative thermal relaxation of fluorophores and their effects on the effective refractive index and grating periodicity of the FBG. The relative change in Bragg wavelength can be represented as follows.

$$\frac{\Delta\lambda_B}{\lambda_B} = (\alpha + \eta)(\Delta T_{\text{non-radiative relaxation}}) \quad (4)$$

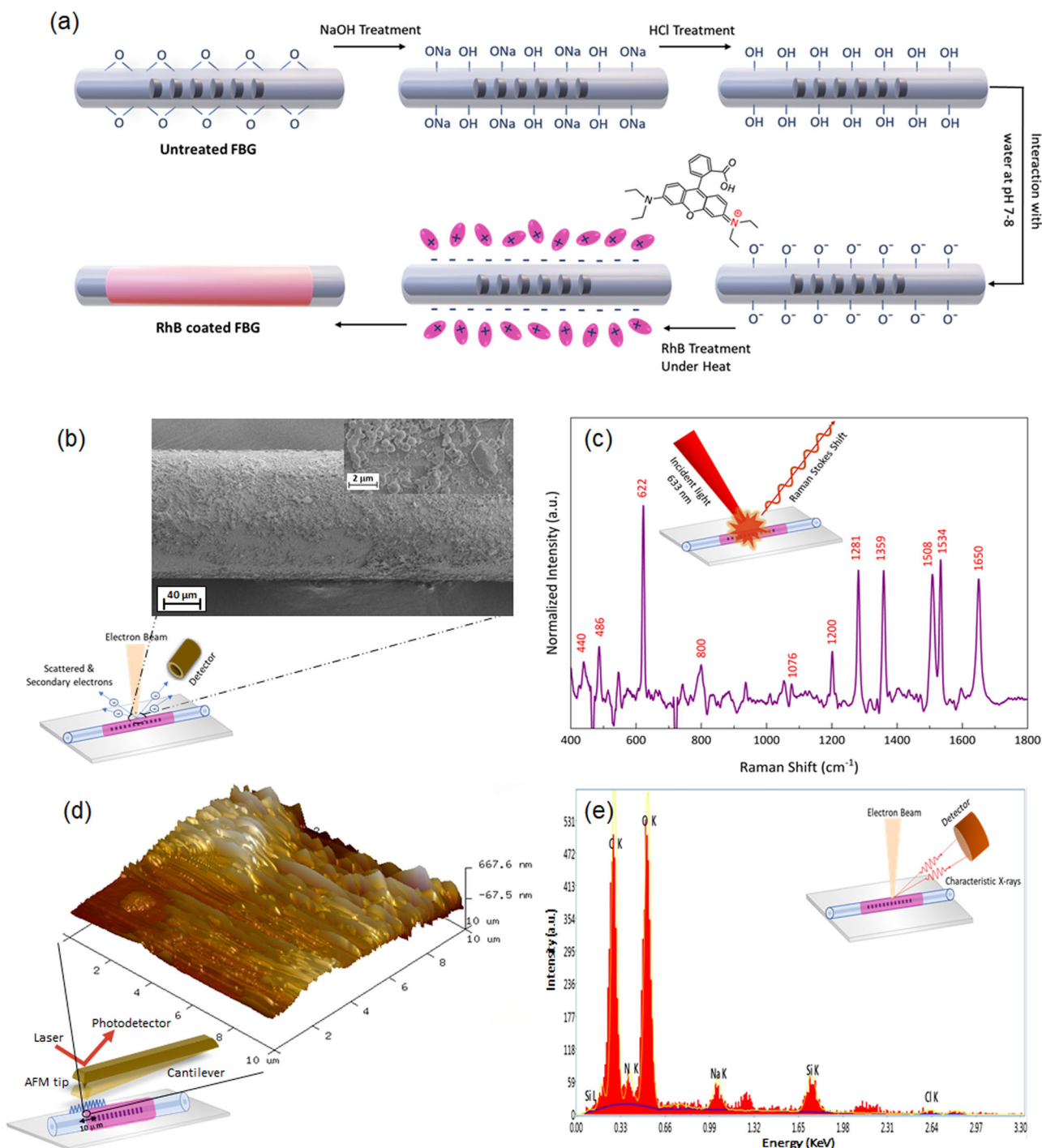


**Fig. 2 | Fabrication and characterization of RhB-coated FBG.** **a** Schematic representation of the process for developing RhB-coated FBG sensor. **b** Scanning electron microscopy image showing the surface morphology of RhB on FBG, **c** Raman spectra representing characteristic vibrational modes of RhB and silica

FBG, **d** 3D projection of RhB adsorbed on FBG imaged with atomic force microscopy displaying the thickness of the coating and **e** energy-dispersive X-ray spectra showing elemental composition of RhB-coated FBG.

where,  $\alpha = (1/\lambda) \left( \frac{\partial \lambda}{\partial T} \right)$  is the thermal-expansion coefficient and  $\eta = (1/n_{\text{eff}}) \left( \frac{\partial n_{\text{eff}}}{\partial T} \right)$  is the thermo-optic coefficient of silica FBG, having approximate values of  $0.55 \times 10^{-6}$  and  $8.6 \times 10^{-6}$  respectively<sup>1</sup>. Since the thermal-expansion coefficient is significantly lower than the thermo-optic coefficient of FBG, Eq. 4 can be further simplified to the following expression, where the relative change in the effective refractive index of the FBG induced by the non-radiative photothermal dissipation of fluorophores

results in a shift in the Bragg wavelength.

$$\frac{\Delta \lambda_B}{\lambda_B} = \left( (1/n_{\text{eff}}) \left( \frac{\partial n_{\text{eff}}}{\partial T} \right) \right) (\Delta T_{\text{non-radiative relaxation}}) \quad (5)$$

**Temperature calibration.** To measure the photothermal relaxation in fluorescent materials, we calibrated the FBG using an infrared camera to establish a relationship between the shift in Bragg wavelength and

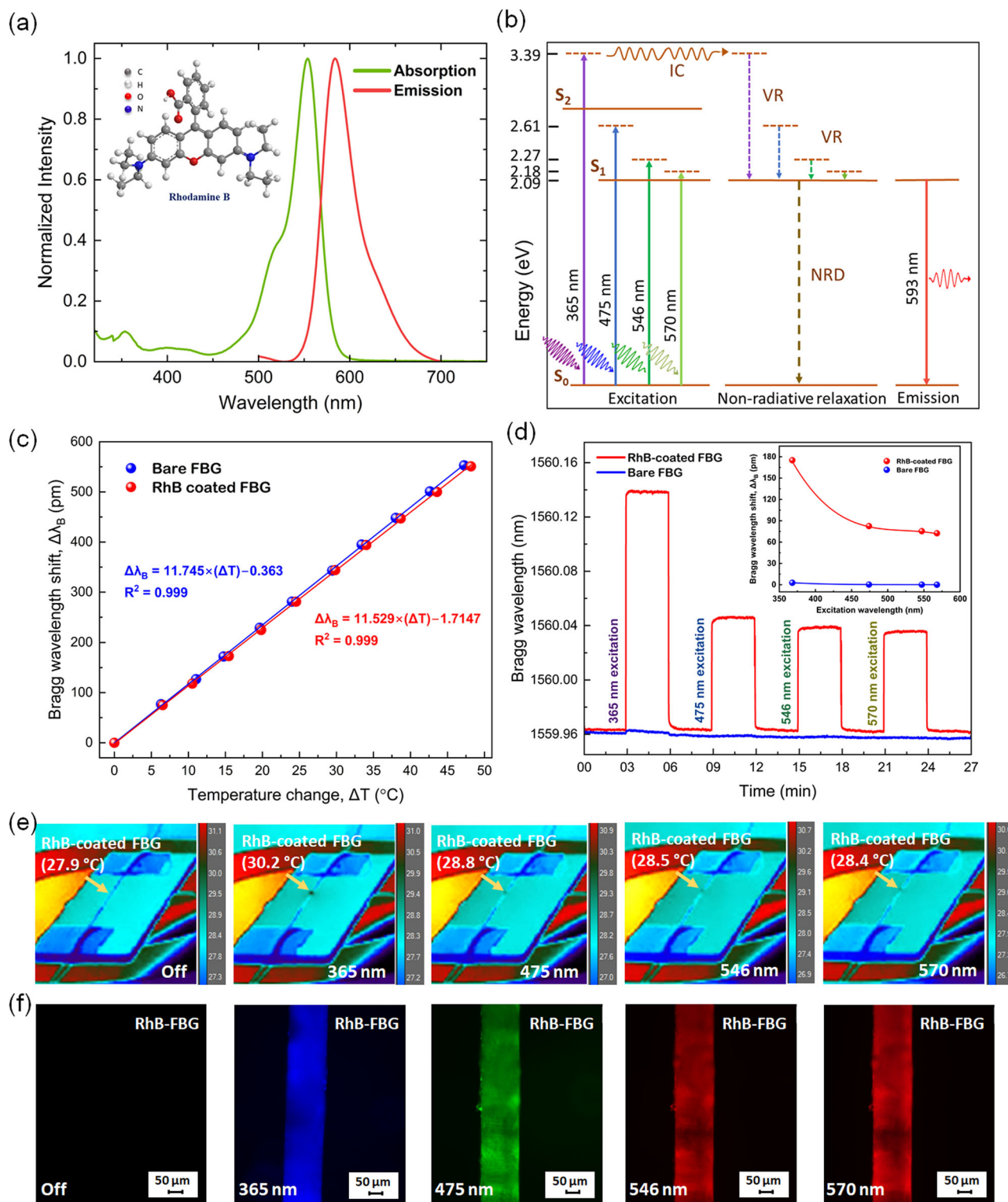


**Fig. 3 | Excitation wavelength-dependent response of RhB-coated FBG.** **a** UV-visible and Photoluminescence spectroscopy results of RhB dissolved in water. Inset: Rhodamine B molecular structure having conjugated double bonds. The absorption and emission spectra overlap with mirror symmetry corresponding to the  $S_0$ - $S_1$  transition. **b** Jablonski diagram depicting the absorption and emission transitions occurring in RhB, along with the energy levels associated with initial vibronic transitions and emission. The solid and dashed horizontal lines represent the electronic and vibrational excited levels, respectively. The initial excitation and non-radiative relaxation processes corresponding to various excitation wavelengths are depicted by solid and dashed vertical lines, respectively. IC internal conversion, VR

vibrational relaxation, NRD non-radiative de-excitation. The colored arrows represent the wavelength of the excitation and emission photons. **c** Temperature calibration curve of FBG sensor before and after RhB coating. **d** Bragg wavelength shift of bare FBG and RhB-coated FBG with respect to various excitation filters (DAPI, FITC, TRITC, and mCherry) at constant irradiance of  $142 \text{ mW cm}^{-2}$  (Inset: Corresponding mean Bragg wavelength shifts of RhB-coated FBG and bare FBG). **e** Thermal images of RhB-coated FBG during its photoexcitation with various excitation filters, indicating the maximum temperature observed. **f** Fluorescence microscope images of RhB-coated FBG sensor with respect to various source excitation filters (DAPI, FITC, TRITC, and mCherry).

temperature change. The same FBG before and after coating with RhB was placed on a hotplate, where the temperature was gradually increased from 25 °C to 75 °C in increments of 5 °C. Simultaneously, the temperature and the Bragg wavelength were recorded using the IR camera and the FBG interrogator, respectively. A corresponding increase in the Bragg wavelength with temperature was observed (Supplementary Fig. 3). The calibration curve (Fig. 3c) displays a linear relationship between the Bragg wavelength shift and temperature change, with a sensitivity of 11.7 pm °C<sup>-1</sup> for bare FBG and 11.5 pm °C<sup>-1</sup> for RhB-coated FBG. The slight variation in sensitivity could be due to the direct transfer of heat through the cladding to the core for bare FBG, while in the case of the RhB-coated FBG, heat diffusion happens through the material-coated cladding into the core. This demonstrates the potential of FBGs as effective optical thermometers, exhibiting a thermal sensitivity of 11.7 pm °C<sup>-1</sup>. To analyze the noise characteristics of the FBG sensor, it was securely mounted on a glass slide and positioned in a stable environment at room temperature. The sensor's response was recorded over a period of approximately 30 min. The inset of Supplementary Fig. 4a presents the time trace of the FBG response. The Allan deviation (Supplementary Fig. 4a) calculated from this time trace indicates a minimum detectable temperature of 3.4 m°C and a sensor noise of 0.017 °C Hz<sup>-1/2</sup> (Supplementary Fig. 4b).

**Excitation photon-wavelength-dependent response.** Since RhB has a broad absorption spectrum, we measured the response of the RhB film to excitation with various wavelength filter configurations covering the absorption spectrum of RhB while maintaining constant excitation intensity for all filters. Figure 3d shows the measured Bragg wavelength shifts after exciting both RhB-coated FBG and bare FBG with DAPI, FITC, TRITC, and mCherry filters having central wavelengths at 365 nm, 475 nm, 546 nm, and 570 nm, respectively (Supplementary Fig. 5a), keeping the illumination intensity constant at 142 mW cm<sup>-2</sup> for all the wavelengths.

When the bare FBG was excited with different wavelengths (Fig. 3d), there was hardly any observed Bragg wavelength shift, except for a shift of approximately 3 pm corresponding to 365 nm excitation. This shift was attributed to the absorption of UV photons by the germania-doped silica fiber core, resulting in changes to the effective refractive index of FBG<sup>63</sup>. It can be observed from Fig. 3d that the RhB-coated FBG sensor experienced a Bragg wavelength shift corresponding to the wavelength or energy of the photons used for excitation. The shorter the wavelength or the higher the energy of the incident photons on the RhB-coated FBG, the more significant the shift in Bragg wavelength. This could be due to the higher level of vibronic transitions caused by excitation with high-energy photons, which leads to more non-radiative dissipation of absorbed energy, resulting in increased localized non-radiative thermal effect on FBG. Whereas the radiative emission begins primarily from the thermally equilibrated state, irrespective of the wavelength or energy of the excitation photons. This is apparent from the fluorescence spectra of RhB-coated FBG (Supplementary Fig. 5b), which displays an emission peak at 593 nm regardless of the excitation filter used. The sensor displayed the highest Bragg wavelength shift of approximately 175 pm in the case of excitation with DAPI filter (365 nm), whereas the Bragg wavelength shifts observed with respect to FITC (475 nm), TRITC (546 nm), and mCherry (570 nm) filter excitation were approximately 82 pm, 75 pm, and 72 pm, respectively. The significant difference in Bragg wavelength shift observed with the DAPI filter compared to other filters can be attributed to the high energy of 365 nm wavelength excitation photons (3.39 eV), causing electronic transitions to the vibrational level (S<sub>2</sub>)<sup>54</sup> much higher than the equilibrated excited state (Fig. 3b). This results in more non-radiative dissipation of absorbed photon energy. In contrast, excitations at 475 nm (2.61 eV), 546 nm (2.27 eV), and 570 nm (2.18 eV) are primarily associated with S<sub>0</sub>-S<sub>1</sub> electronic transitions<sup>53,54</sup>. The energy values associated with these vibronic transitions at different excitation wavelengths, along with the extent of non-radiative transitions and the energy associated with the radiative emission process, are illustrated in

Fig. 3b. Therefore, the Bragg wavelength shift could be indicative of the extent of vibrational transitions or non-radiative energy dissipation involved in the fluorescence process. In this study, the self-heating of the FBG caused by the absorption of probe infrared light (150–200 μW) is considered negligible, as confirmed by the Bragg wavelength data recorded over a 30-min period by the interrogator (Supplementary Fig. 6).

The thermal data of RhB-coated FBG (Fig. 3e, Supplementary Fig. 7a) recorded using the thermal IR camera (FLIR E95) during its photoexcitation with all the wavelengths indicate a decreasing trend in the temperature rise of the coated fluorophores in relation to the excitation photon energy. This trend aligns with the results obtained from the calibrated FBG, as shown in Supplementary Fig. 7b. Conversely, no temperature rise has been observed in the case of bare FBG when excited with different wavelength photons (Supplementary Fig. 7c, d). The corresponding fluorescence microscope images captured with all the filters for both RhB-coated FBG and bare FBG are shown in Fig. 3f, Supplementary Fig. 7e, respectively. The fluorescence characteristics of rhodamine, which emits around 593 nm (Supplementary Fig. 5b), are visible with all the filters, each displaying a pseudo-colored fluorescence image based on the emission barrier spectrum of the specific filter. Conversely, no fluorescence was observed when excited with any of the filters for the bare FBG (Supplementary Fig. 7e).

We have further verified the FBG technique for investigating the photoresponse of RhB in solution form. Instead of coating the FBG, 10–15 μL of RhB dye solution (dissolved in DI water) at concentrations of 1700 μM, 380 μM, and 130 μM was dropped on the FBG, which was mounted on a glass slide and positioned on the microscope stage. Corresponding Bragg wavelength shifts recorded while exposing the solution to various excitation wavelengths using DAPI, FITC, TRITC, and mCherry filters, all at a constant irradiance of 142 mW cm<sup>-2</sup>, are shown in Fig. 4. Similar to that of RhB film, it was found that at a higher concentration of RhB solution (1700 μM), the Bragg wavelength shift was influenced by the wavelength or energy of the excitation photons (Fig. 4a, b). The maximum Bragg wavelength shift of 50 pm was observed when excited with 365 nm photons, whereas for excitation at 475 nm, 546 nm, and 570 nm, the Bragg wavelength shifts were nearly the same, around 27 pm, 26.5 pm, and 26.7 pm, respectively. Conversely, as the concentration of the RhB solution decreased to 380 μM and 130 μM, the Bragg wavelength shift began to align more closely with the absorption characteristics of RhB (Fig. 4c, d). To understand the observed phenomena, we analyzed the UV-visible absorption characteristics of RhB at various concentrations, as illustrated in Supplementary Fig. 8. As previously reported<sup>39</sup>, with an increase in concentration, the primary absorption band broadens, and the intensity of the secondary absorption band in the near UV wavelength region gradually increases; there is little difference in the absorption characteristics concerning wavelength when the concentration reaches around 4000 μM, as stated before<sup>64</sup>. This could be due to the reduced likelihood of photons escaping as the concentration of the solution rises. Hence, considering equivalent absorbance irrespective of the excitation wavelengths used, the Bragg wavelength shifts observed at a concentration of 1700 μM likely reflect the extent of vibronic transitions occurring in photoexcited RhB molecules. The significant Bragg wavelength shift observed at 365 nm may be attributed to vibronic transitions to a higher excited electronic state (S<sub>2</sub>)<sup>54</sup>, leading to more non-radiative photothermal dissipation when the molecules return to the ground state. Whereas, for the excitation wavelengths 475 nm, 546 nm, and 570 nm, the electronic transitions occur to the first excited state (S<sub>1</sub>)<sup>53,54</sup>, resulting in less photothermal dissipation as the molecules revert to the ground state. Conversely, the Bragg wavelength shift aligning with the absorption characteristics of RhB solution at 130 μM and 380 μM concentrations can be attributed to the increased likelihood of photon escape, resulting in more pronounced shifts at wavelengths with higher absorption probabilities (hence enhanced non-radiative photothermal dissipation), such as at 546 nm excitation wavelength. Despite the lower absorption probability observed at both 365 nm and 475 nm excitation wavelengths (Supplementary Fig. 8), the higher Bragg wavelength shift noted at 365 nm excitation (Fig. 4c), which progressively approaches the shift associated with

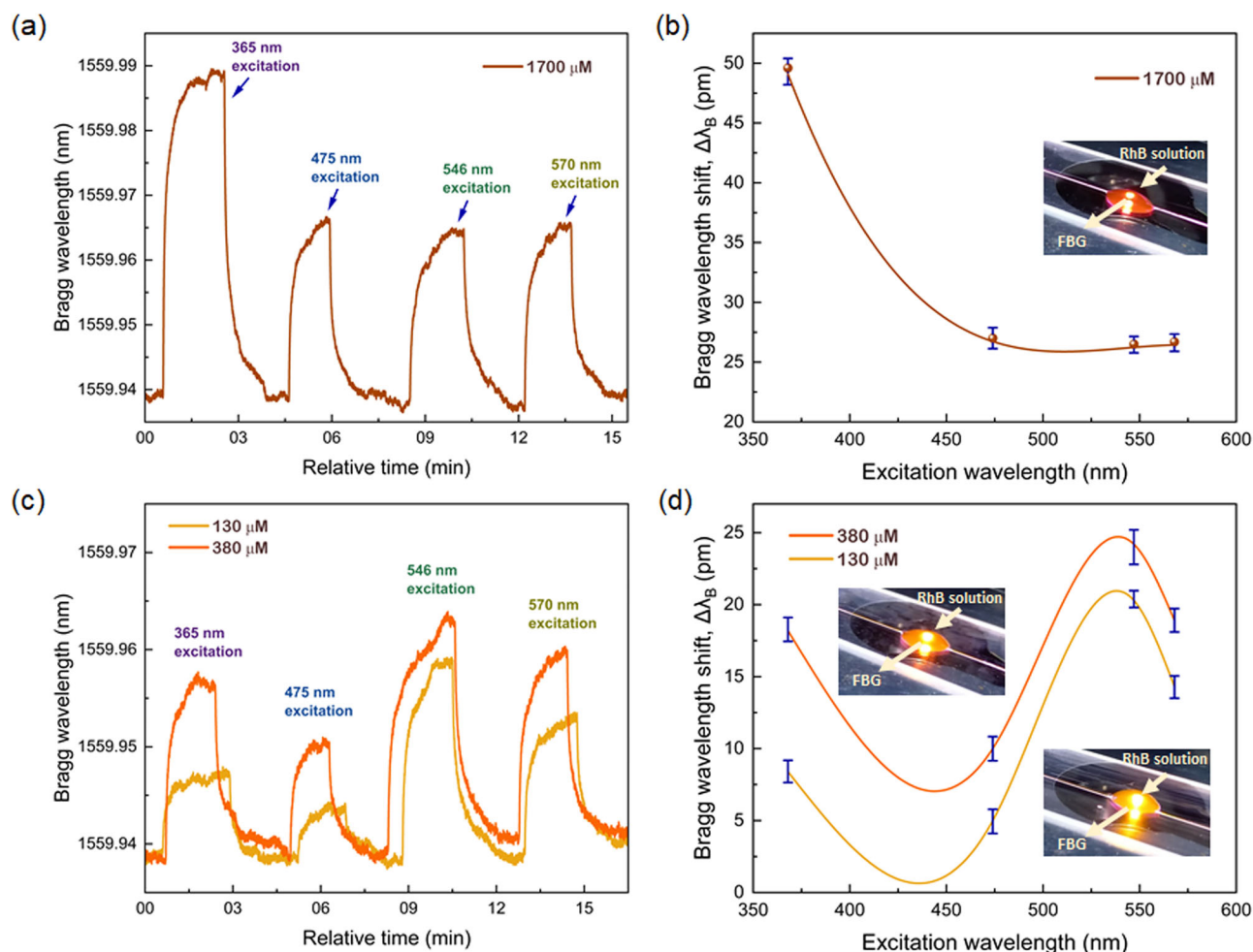


**Fig. 4 | Excitation wavelength-dependent response of different concentrations of RhB solution captured with FBG.** **a** Bragg wavelength shifts measured for 1700  $\mu\text{M}$  RhB solution with respect to various excitation filters (DAPI, FITC, TRITC, and mCherry) at constant irradiance of  $142 \text{ mW cm}^{-2}$ . **b** Corresponding mean Bragg wavelength shifts (The error bar represents the maximum deviation from the mean Bragg peak). **c** Bragg wavelength shifts measured for 380  $\mu\text{M}$  & 130  $\mu\text{M}$  RhB solution

during photoexcitation with various excitation filters (DAPI, FITC, TRITC, and mCherry) at constant irradiance of  $142 \text{ mW cm}^{-2}$ . **d** Corresponding mean Bragg wavelength shifts (The error bar represents the maximum deviation from the mean Bragg peak). The inset photographs in (b) and (d) show the photoexcitation of a RhB solution dropped on the FBG, which is positioned on a glass slide on top of the fluorescence microscope stage.

the primary absorption peak at 546 nm as the concentration increases to 380  $\mu\text{M}$ , may be attributed to a higher electronic level of transition associated with 365 nm excitation compared to excitation at the primary absorption band (spanning 475 nm, 546 nm, and 570 nm), leading to more non-radiative dissipation of absorbed photon energy.

Thus, the results indicate that the FBG technique can provide insights into both the molecular absorption characteristics and the level of vibronic transitions occurring in fluorescent molecules through non-radiative photo-thermal relaxation as reflected in Bragg wavelength shifts. The absorption information holds true for low concentrations of the solution, while information about vibronic transitions can be obtained when the molecular absorbance is similar across the excitation wavelengths, as demonstrated by the Bragg wavelength shifts observed under 365 nm and 475 nm excitation, or in higher concentrations of RhB solution and RhB film. Such capabilities could open up new avenues for molecular spectroscopy utilizing fiber Bragg grating technology.

The thermal information obtained from the IR camera (FLIR E95) during the photoexcitation of a high concentration (1700  $\mu\text{M}$ ) and a low-concentration (100  $\mu\text{M}$ ) RhB solution is shown in Supplementary Fig. 9b and d, respectively. The thermal data correspond perfectly with the Bragg wavelength shifts observed at various excitation wavelengths for each concentration (Supplementary Fig. 9a, c), indicating the successful capture

of photothermal information by the FBG. Additionally, the fluorescence spectra for both the low- and high-concentration RhB solutions are presented in Supplementary Fig. 10.

The Bragg wavelength spectra recorded from FBG during the photoexcitation of the RhB film and RhB solution at various wavelengths are presented in Fig. 5. For both the RhB film (Fig. 5c) and the high concentration (1700  $\mu\text{M}$ ) RhB solution (Fig. 5d), a noticeable evolution of the Bragg spectral split was observed as the excitation photon energy increased, with the RhB film exhibiting more intense spectral splitting. This could be due to the highly localized and enhanced thermal generation induced by high-energy photons striking the approximately 2.1 mm (spot diameter) grating region of the RhB-coated FBG, which subsequently transfers to the non-irradiated grating region, creating a temperature gradient and hence a refractive index gradient along the grating axis. As a result, the reflected Bragg wavelength under the irradiated grating region differs significantly from that under the non-irradiated grating region, leading to a pronounced split in the Bragg wavelength spectrum<sup>65</sup>. In contrast, for the RhB solution, while a prominent spectral split is observed with high-energy photon excitation (Bottom inset of Fig. 5d), the heat generated from the photomolecule interaction on the grating region of the FBG becomes less localized due to thermal diffusion, resulting in a less intense split. The excitation wavelength-dependent spectral split gradually becomes less discernible with

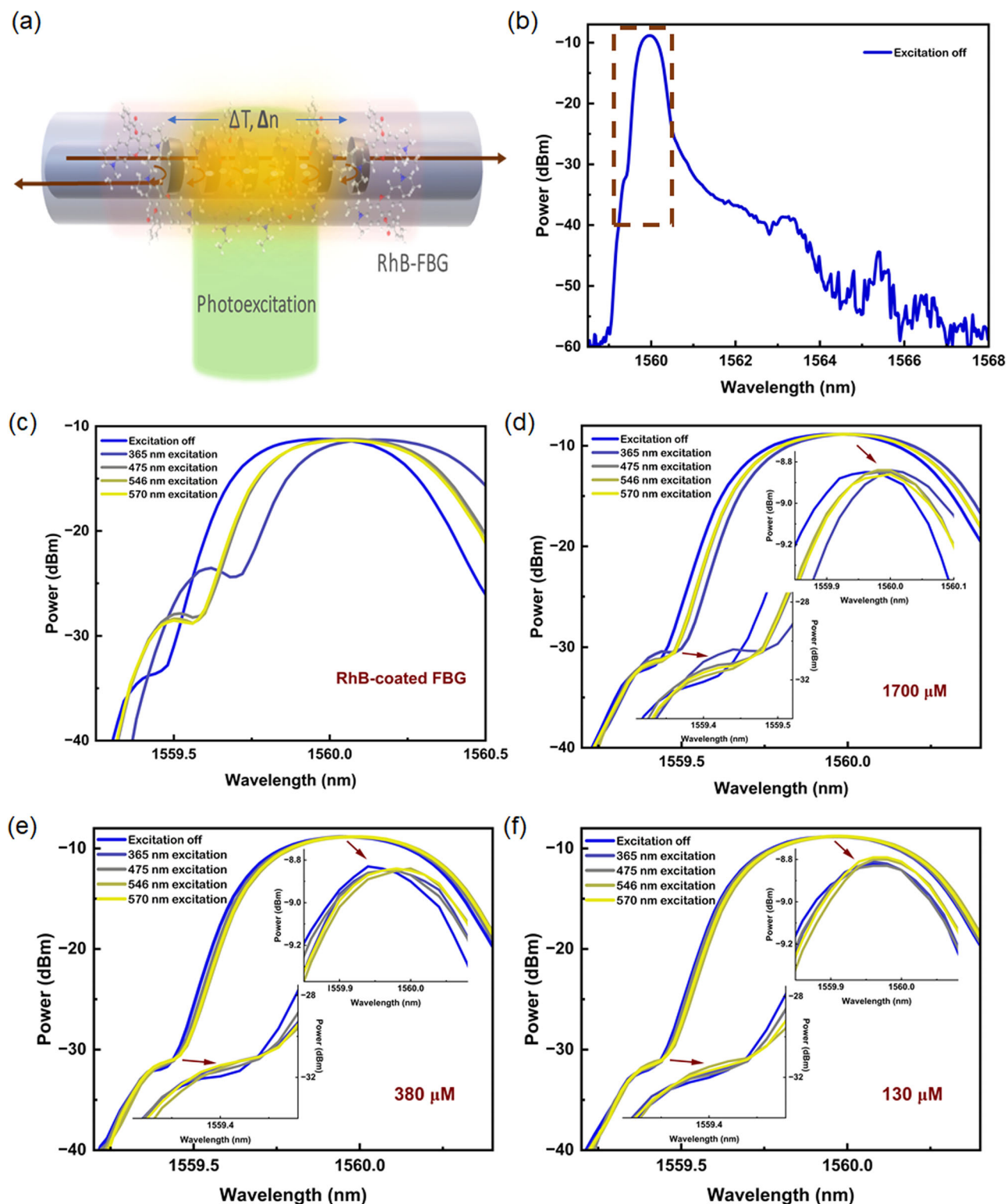


**Fig. 5 | Excitation wavelength-dependent response of RhB film & different concentrations of RhB solution captured in the Bragg wavelength spectrum.** a Schematic representing localized photothermal generation during the interaction of photons with RhB molecules. b Bragg wavelength spectrum captured from FBG when photoexcitation is off. The dashed box highlights the section of the spectrum displayed in subsequent figures. c Bragg wavelength spectrum captured from FBG

during photoexcitation of RhB film with various excitation filters (DAPI, FITC, TRITC, and mCherry) at constant irradiance of  $142 \text{ mW cm}^{-2}$ . Bragg wavelength spectrum captured from FBG during photoexcitation of different concentrations of RhB solution: d 1700  $\mu\text{M}$ , e 380  $\mu\text{M}$ , and f 130  $\mu\text{M}$  with various excitation filters (DAPI, FITC, TRITC, and mCherry) at constant irradiance of  $142 \text{ mW cm}^{-2}$ .

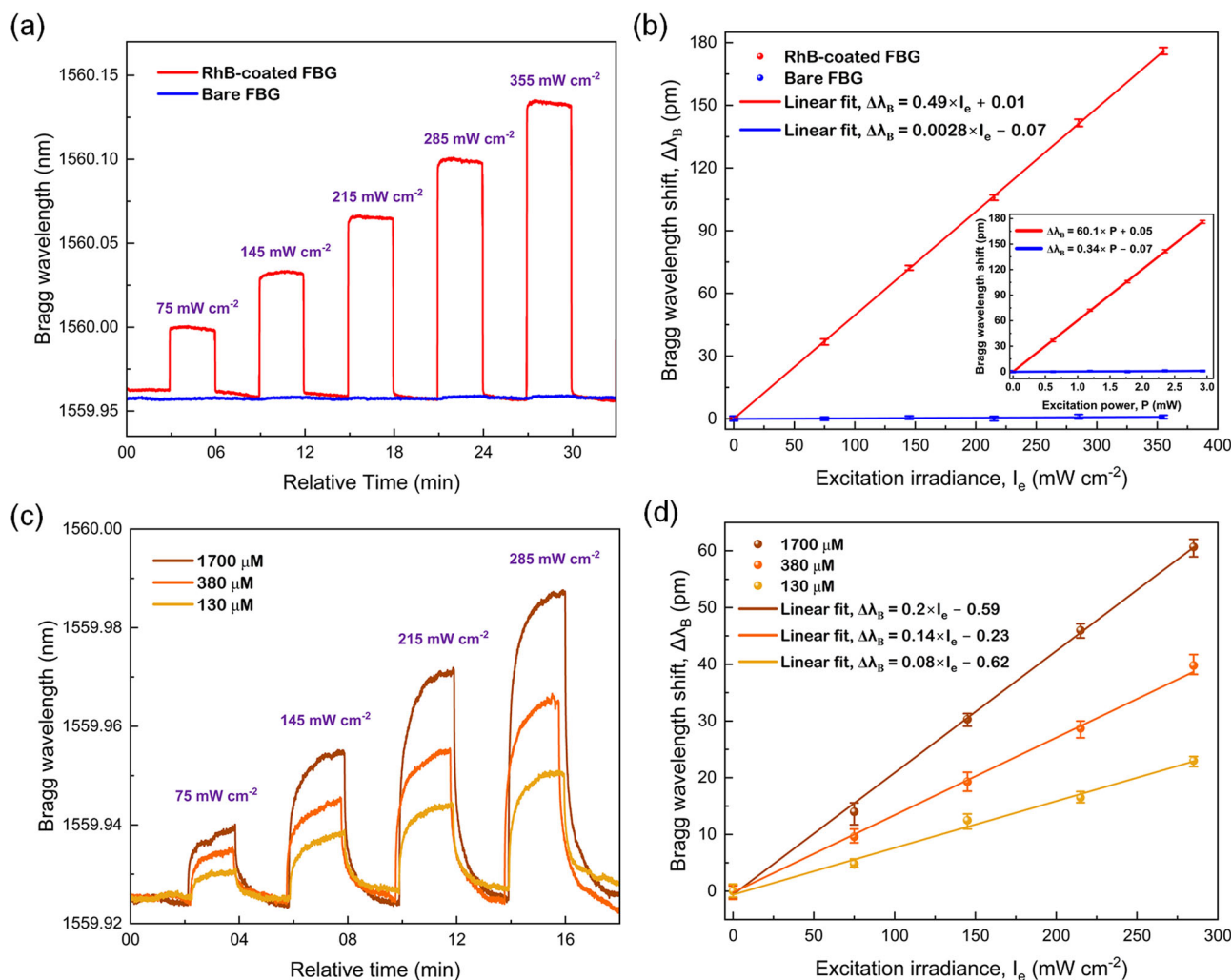


**Fig. 6 | Excitation intensity-dependent response of the RhB film and different concentrations of RhB solution captured with FBG. a** Bragg wavelength shift of bare FBG and RhB-coated FBG with respect to various excitation intensities from 570 nm wavelength filter (mCherry). **b** Corresponding mean Bragg wavelength shifts with respect to different excitation intensities & incident excitation powers (Inset graph) representing linear characteristics (The error bar represents the

maximum deviation from the mean Bragg peak). **c** Bragg wavelength shifts measured from FBG during photoexcitation of different concentrations of RhB solution with various excitation intensities from 570 nm wavelength filter. **d** Corresponding mean Bragg wavelength shifts with respect to different excitation intensities representing linear characteristics (The error bar represents the maximum deviation from the mean Bragg peak).

decreasing concentrations of the RhB solution (380  $\mu\text{M}$  (Fig. 5e) and 130  $\mu\text{M}$  (Fig. 5f)). Nonetheless, a slightly more intense split was observed for 546 nm excitation, followed by 570 nm excitation in both cases (Bottom inset of Fig. 5e, f), indicating greater thermal generation at these wavelengths due to enhanced photon absorption. No such progression in spectral splitting was evident for the bare FBG (Supplementary Fig. 11). This study presents an approach to capturing photothermal generation and its localization in fluorescent materials by monitoring the progression of the Bragg spectral split.

**Excitation photon-intensity-dependent response.** Next, we captured the response of the RhB film to different optical excitation intensities from the LED source by measuring the corresponding change in the Bragg wavelength, shown in Fig. 6a, b. In this experiment, both RhB-coated FBG and bare FBG were exposed to various optical irradiances (75, 145, 215, 285, and 355  $\text{mW cm}^{-2}$ ) from LED fluorescence microscope light source through 570 nm excitation filter (mCherry) and the corresponding excitation power incident on the grating region of FBG (spot diameter  $\sim 2.1$  mm) was calculated to be approximately 0.62 mW, 1.19 mW, 1.77 mW, 2.35 mW, and 2.93 mW respectively. There was hardly any Bragg wavelength shift observed when the bare FBG was

photoexcited with different intensities, where a maximum shift of  $\sim 1.2$  pm was observed for an excitation irradiance of 355  $\text{mW cm}^{-2}$ . Conversely, the maximum Bragg wavelength shift of  $\sim 175$  pm was observed with RhB-coated FBG at an excitation irradiance of 355  $\text{mW cm}^{-2}$  (2.93 mW incident excitation power). Even at a low excitation irradiance of around 75  $\text{mW cm}^{-2}$  (620  $\mu\text{W}$  incident excitation power), there was a shift of approximately 37 pm in the Bragg wavelength. With the increase in excitation intensity or power, our experimental study demonstrated a corresponding increment in Bragg wavelength shift on account of the increased number of photon-molecule interactions, resulting in more excited state transitions followed by non-radiative and radiative de-excitations<sup>66</sup>. The sensor exhibited a linear shift in Bragg wavelength with respect to the excitation intensity (Fig. 6b) or power (Inset of Fig. 6b), representing the high linearity of the sensor. The photoinduced Bragg wavelength sensitivity of the sensor calculated from the linearity graph is  $\sim 0.5$  pm  $\text{mW}^{-1}$   $\text{cm}^{-2}$  (60 pm  $\text{mW}^{-1}$ ), which indicates the potential of the sensor in capturing non-radiative photothermal generation with an excitation intensity of about 2  $\text{mW cm}^{-2}$  ( $\sim 17$   $\mu\text{W}$  incident excitation power). This can be improved by etching the cladding or using a high-resolution FBG interrogator with sub-picometer resolution. The measured Bragg wavelength data from the bare FBG (Fig. 6a,

b), which showed hardly any shift, confirm that no photon-induced thermal effect is involved from the source, even after exposure to an irradiance of  $355 \text{ mW cm}^{-2}$ . The thermal data obtained from the non-contact IR camera (FLIR E95) based temperature measurement of RhB-coated FBG during photoexcitation at various intensities displays an increase in the localized temperature corresponding to rising excitation intensity (Supplementary Fig. 12a, c). Whereas no such temperature increase was observed with bare FBG (Supplementary Fig. 12b, d).

We further explored the response of the RhB solution to different photoexcitation intensities. Figure 6c, d illustrates the shift in Bragg wavelength observed when different concentrations of RhB solution were dropped on FBG and exposed to various optical irradiances using the 570 nm excitation filter. The Bragg wavelength increased with both the intensity of photoexcitation and the concentration of the RhB solution. This could be due to a higher concentration of molecules allows for more interactions with photons, reducing the chances of photons escaping. Conversely, at lower concentrations, more photons have the opportunity to escape, leading to reduced non-radiative thermal dissipation resulting from fewer photon-molecule interactions. While a linear increase in Bragg wavelength shift was evident concerning excitation intensity across all the concentrations (Fig. 6d), the photo-induced Bragg wavelength sensitivity was greater at higher concentrations:  $0.2 \text{ pm mW}^{-1} \text{ cm}^{-2}$  for  $1700 \mu\text{M}$ , followed by  $0.14 \text{ pm mW}^{-1} \text{ cm}^{-2}$  for  $380 \mu\text{M}$ , and  $0.08 \text{ pm mW}^{-1} \text{ cm}^{-2}$  for  $130 \mu\text{M}$ . This can be attributed to the greater localized photothermal generation in the vicinity of the FBG cladding at high concentrations. In contrast, at lower concentrations, the photothermal effect becomes less localized due to faster thermal diffusion. This illustrates the sensor's capability to detect photothermal generation at lower excitation intensities as the concentration or photothermal localization increases. This is evidenced by the required excitation intensities of  $5 \text{ mW cm}^{-2}$  for  $1700 \mu\text{M}$  solution,  $7 \text{ mW cm}^{-2}$  for  $380 \mu\text{M}$  solution, and  $12.5 \text{ mW cm}^{-2}$  for  $130 \mu\text{M}$  RhB solution using 570 nm wavelength filtered LED excitation. The thermal data (Supplementary Fig. 13) collected from the IR camera (FLIR E95) during the photoexcitation of RhB solutions at different concentrations on the FBG show an increase in localized temperature with higher excitation intensities across all concentrations. Further, the rise in localized temperature is more significant at higher concentrations.

The corresponding Bragg wavelength spectrum (Supplementary Fig. 14) recorded from the FBG during the photoexcitation of the RhB film and RhB solution at various irradiances reveals the evolution of spectral split in relation to increasing optical irradiance. This could be due to the rise in non-radiative photothermal generation, resulting from a greater number of photon-molecule interactions at higher excitation optical irradiance levels. In contrast, no progression in spectral split was observed with the bare FBG (Supplementary Fig. 14b). Notably, the Bragg spectral split is more pronounced for the RhB film (Supplementary Fig. 14c), diminishing as the concentrations of the RhB solution decrease (Supplementary Fig. 14d–f) due to increased thermal diffusion, which leads to less localized photothermal generation.

Moreover, the sensitivity of detecting the photon-induced non-radiative thermal relaxation of fluorescent dye RhB was compared between the FBG technique and the IR camera. Figure 7 shows a comparison of the temperature rise obtained from the calibrated FBG and that recorded by the IR camera during photoexcitation of RhB, both in solution and in thin film form, at different intensities through 570 nm filter. The temperature rise ( $\Delta T$ ) observed for  $130 \mu\text{M}$  RhB solution with the FBG technique closely aligns with the results obtained from the IR camera (Fig. 7d). However, as the concentration increases, the sensitivity becomes higher for FBG than for the IR camera (Fig. 7c, b). When detecting the photothermal effect in the thin film, a significant discrepancy in  $\Delta T$  was observed between the two techniques, with the FBG method demonstrating greater sensitivity (Fig. 7a). This can be due to faster thermal diffusion in the solution as the concentration decreases, which disperses heat from the hotspot toward the surroundings, allowing the IR camera to capture it effectively (as shown in Supplementary Fig. 15). In contrast, for the thin film, the relatively poor

thermal conductivity of air compared to that of silica fiber causes the photon-induced heat generated on the surface of the FBG to mostly diffuse toward its core rather than dissipate into the surrounding air. Consequently, the limitation of the IR camera to only surface or macroscopic temperature measurement with low spatial resolution makes it unable to capture the actual local photothermal changes occurring at a micro scale on the surface of the  $125 \mu\text{m}$  diameter FBG cladding (Supplementary Fig. 15a). Whereas the inherent micron size of the FBG makes it well-suited to capture the transient non-radiative localized thermal changes resulting from vibronic transitions in fluorophores. This capability can potentially unveil new opportunities for investigating localized photon-induced thermal generation using fiber Bragg grating technology. Additionally, we have evaluated the photoresponse of RhB-coated FBG over time for a period of more than a year (Supplementary Fig. 16), demonstrating the durability of the photothermal sensing approach over the long term.

## Conclusion

In summary, we have demonstrated a method of probing photon-induced non-radiative thermal relaxation in fluorophores, using the FBG sensor. The study was carried out using a common fluorescent organic dye, Rhodamine B, where RhB, either coated on FBG in the form of a film or dropped on the FBG in the form of a solution, was exposed to the desired excitation wavelength through the excitation filter of the fluorescence microscope equipped with a broadband LED light source. The fluorescence phenomenon was observed with the microscope, while the photon-induced thermal effect was simultaneously captured with the FBG. In the case of the RhB film and high concentration RhB solution, the Bragg wavelength shift was observed to be dependent on the energy of the excitation photons, reflecting the extent of vibronic transitions based on non-radiative photothermal dissipation in response to the wavelength of excitation. Whereas in the case of a low-concentration RhB solution, the Bragg wavelength shifts observed at different excitation wavelengths follow its absorption characteristics. Further, the FBG technique was able to provide insight into the vibronic transition level in low-concentration RhB solution, provided that it has equivalent molecular absorbance across photoexcited wavelengths, as evidenced by the Bragg wavelength shifts obtained at the low probability absorption region. The photoexcitation intensity-dependent response showed a linear shift in the Bragg wavelength in relation to the variation in incident excitation intensity, representing the high linearity of the sensor for the quantitative study of photothermal generation. The photons induced Bragg wavelength sensitivity, which was highest for the RhB film, followed by a higher concentration of RhB solution, gives an insight into the localization of the thermal effect generated from photon-molecule interaction. This demonstrates the potential of the FBG in capturing photothermal information in fluorescent molecules with an excitation intensity of less than  $5 \text{ mW cm}^{-2}$  from an LED source, owing to increased photothermal localization and the linear characteristic of the sensor. Furthermore, a comparison of the FBG technique with the IR camera highlights the advantages of the proposed approach over traditional thermometry methods in detecting micron-scale localized transient non-radiative thermal changes caused by photon-induced molecular vibronic transitions. Further, the Bragg wavelength spectrum captured from FBG during photoexcitation of RhB film and different concentrations of RhB solution at different wavelengths and intensities shows a distinct approach of probing photothermal generation and its extent of localization by means of modulation in the Bragg spectral split. This Bragg wavelength shift and Bragg spectral split modulation technique used to capture the photothermal relaxation of fluorophores offers a unique approach that can provide internal thermal information arising from photon-molecule interaction across a wide range of excitation wavelengths and excitation intensities, overcoming the limitations of current thermometry techniques, and hence can be applied in molecular spectroscopy and photon-biomolecular probing applications. Factors that may influence the thermal information captured by FBG, such as self-heating from the absorption of probe infrared light and thermal conduction along the optical fiber, require careful characterization to mitigate these

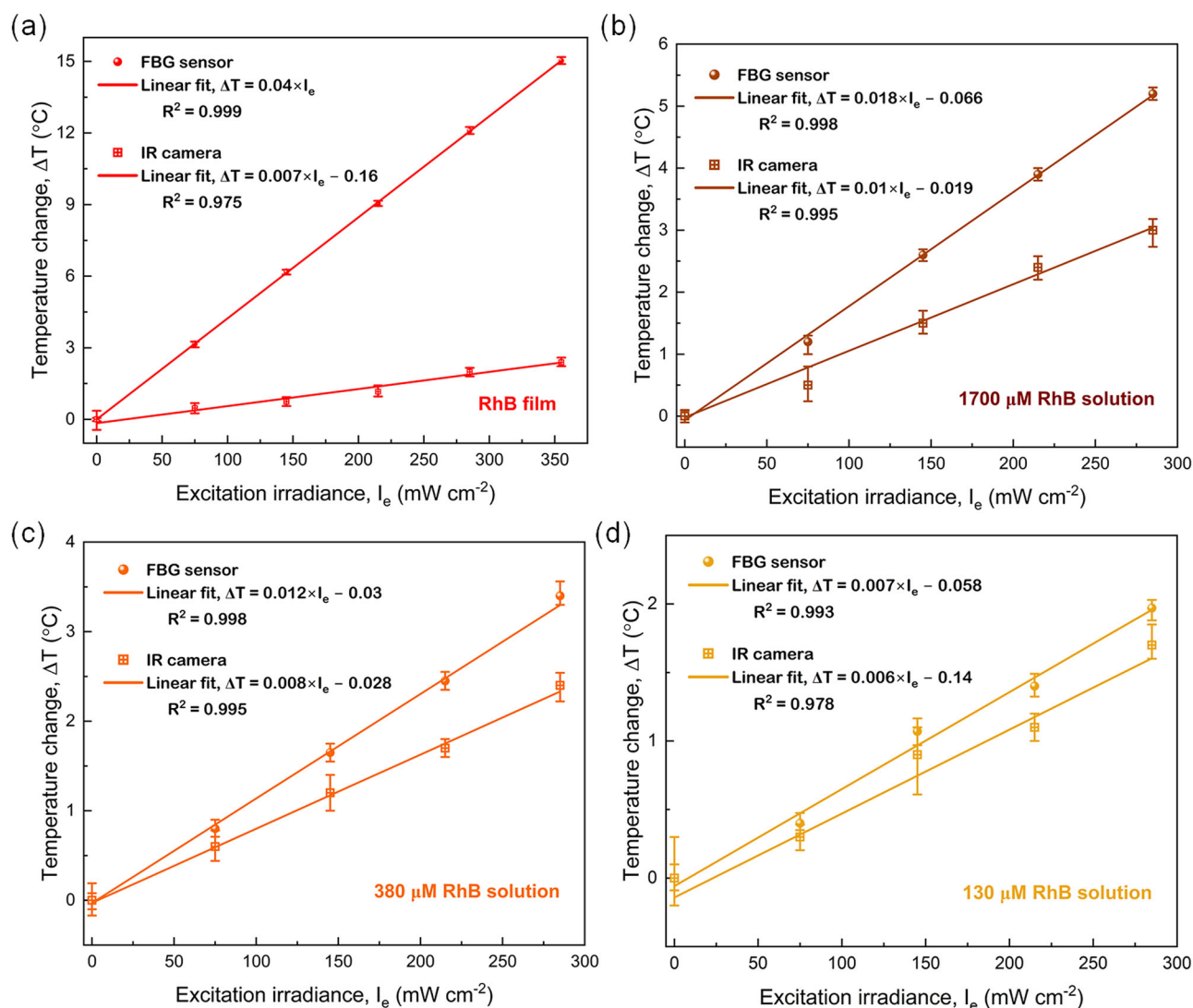


**Fig. 7 | Comparison of the photothermal sensitivity between the FBG technique and the IR camera.** a Temperature changes observed with the FBG sensor and the IR camera during photoexcitation of RhB film at various intensities through 570 nm wavelength filter (mCherry). Temperature changes observed with the FBG sensor

and the IR camera during photoexcitation of different concentrations of RhB solution: **b** 1700  $\mu\text{M}$ , **c** 380  $\mu\text{M}$ , and **d** 130  $\mu\text{M}$  at various intensities through the mCherry filter.

effects. Further comprehensive studies are necessary to gain a deeper understanding of the photon-molecule interaction and its impact on grating parameters and the Bragg wavelength using different fluorescent materials and exciting them at various wavelengths, which could then potentially lead to the development of a novel spectroscopic technique.

## Methods

### Details of the equipment used

A standard IX83 Olympus inverted fluorescence microscope was used, which contains an epifluorescence illumination from a LED light source (CoolLED pE-300<sup>white</sup>) accompanied by different fluorescent filters for DAPI (narrow band UV excitation, with excitation filter BP360-370, dichroic beamsplitter DM410, barrier (emission) filter BA420-460), FITC (narrow band blue excitation, with excitation filter BP470-495, dichroic beamsplitter DM505, barrier (emission) filter BA510-550), TRITC (narrow band green excitation, with excitation filter BP540-550, dichroic beamsplitter DM570, barrier (emission) filter BA575-625), and Mcherry (with excitation filter BP565-585, dichroic beamsplitter DM595, barrier (emission) filter BA600-690). For all the experiments, the microscope objective was set at 20x (Olympus LUCPLFN, 0.45 NA). The fluorescence microscope image was captured using ORCA-Flash 4.0 V3 sCMOS camera (82%

QE). Bragg wavelength measurements were performed with a commercially available high-resolution optical FBG interrogator (LUNA, Hyperion si155). The optical intensity from the excitation source falling on the FBG sensor was measured using a standard Si photodiode power sensor (S120VC, THORLABS) and optical power meter (PM100D, THORLABS). By considering the area of the FBG exposed to photoexcitation as  $2\pi rh$ , where  $r$  denotes the radius of the optical FBG (62.5  $\mu\text{m}$ ), and  $h$  represents the spot diameter ( $\sim 2.1$  mm), the corresponding optical power incident on the FBG was calculated.

### Fabrication of RhB-coated FBG

Firstly, the organic impurities from the surface of the FBG were removed by dipping it in Piranha solution ( $\text{H}_2\text{SO}_4:\text{H}_2\text{O}_2$  at 3:1 molar ratio) for 15 min, then rinsing it with DI water. The sensor was then treated with 0.2 N NaOH (aq.) solution at 40  $^\circ\text{C}$  for 3.5 h and next at room temperature (25  $^\circ\text{C}$ ) for 30 min, followed by DI water wash to remove remnant NaOH (aq.) from the surface of the sensor. The NaOH treatment makes the surface of the fiber more hydrophilic by creating silanol (Si-OH) groups along with the formation of silanol salt groups (Si-ONa) on the fiber surface<sup>45</sup>. After this, the sensor was kept in HCl (aq.) solution (3% (vol.)) at room temperature for 10 min, followed by a DI water rinse. The hydrogen ions in hydrochloric

acid replace the sodium ions and convert all silanol-salt groups on the surface of FBG into silanol groups, which subsequently become deprotonated under DI water treatment, making the fiber surface negatively charged<sup>45</sup>. Finally, the Rhodamine B dye solution (Rhodamine B dissolved in DI water) was drop-casted on functionalized FBG (placed in a grooved Teflon block), and the temperature was maintained at 60–70 °C until the solution was completely dried and adhered to the fiber surface.

### Characterization

**SEM and EDX.** The scanning electron microscope (SEM) image and energy-dispersive X-ray (EDX) spectra of the Rhodamine B-coated FBG were acquired using the Zeiss EVO 18 electron microscope. To prepare the sample, a small portion of the RhB-coated FBG was precisely cut and placed on a stub with the help of carbon tape, which was then sputter-coated with gold to ensure optimal imaging.

**Raman spectroscopy.** The Raman spectra of RhB-FBG were acquired using Jobin Yvon Horiba (HR800) Raman spectrometer equipped with an Olympus BX41 microscope and a CCD detector. The Rhodamine B-coated FBG, affixed to a glass slide, was placed on the microscope stage. A 632 nm He-Ne laser was focused onto it through a 50x objective lens. The spectrum was recorded using a 1800 lines/mm grating, with an exposure time of 1 s and 10 accumulations. The acquired spectrum was then subjected to baseline correction and normalization [0,1] using OriginPro 2024, effectively eliminating background fluorescence.

**AFM imaging.** The AFM image was obtained from Bruker AFM (Dimension ICON with ScanAsyst). A small piece of Rhodamine B-coated FBG was attached to the stub with the help of a glue sticker, and the image was acquired by scanning the RhB-FBG in tapping mode using an RTE-SP-300 tip with a spring constant of 40 N/m. The topographic images were analyzed using Nanoscope Analysis software.

**UV-Vis and fluorescence spectroscopy.** The UV-visible absorption spectrum of Rhodamine B dye dissolved in water was measured by a Jasco V-570 UV/VIS/NIR Spectrophotometer, with the dye solution contained in a 1 cm quartz cell. The emission spectrum of the same solution was measured using a Jasco FP-6600 Spectrofluorometer at an excitation wavelength of 550 nm.

### Data availability

The data that support the findings of this study are available from the corresponding author upon reasonable request.

Received: 10 January 2025; Accepted: 26 December 2025;

Published online: 10 January 2026

### References

- Othonos, A. Fiber Bragg gratings. *Rev. Sci. Instrum.* **68**, 4309–4341 (1997).
- Othonos, A., Kalli, K. & Kohnke, G. E. Fiber Bragg gratings: fundamentals and applications in telecommunications and sensing. *Phys. Today* **53**, 61–62 (2000).
- Liu, Z. & Tam, H.-Y. Industrial and medical applications of fiber Bragg gratings (Invited Paper). *Chin. Opt. Lett.* **14**, 120007 (2016).
- Rohan, R., Venkadeshwaran, K. & Ranjan, P. Recent advancements of fiber Bragg grating sensors in biomedical application: a review. *J. Opt.* **53**, 282–293 (2024).
- Villanueva, G. E. et al. Linear and nonlinear optical properties of carbon nanotube-coated single-mode optical fiber gratings. *Opt. Lett.* **36**, 2104 (2011).
- Shao, L.-Y., Jakubinek, M. B., Sun, T., Simard, B. & Albert, J. Four-wave mixing in carbon nanotube-coated optical fiber gratings. *Appl. Phys. Lett.* **100**, 071108 (2012).
- Shivananju, B. N., Suri, A., Asokan, S. & Misra, A. Carbon nanotube coated fiber Bragg grating for photomechanical optic modulator. *Rev. Sci. Instrum.* **84**, 095101 (2013).
- Shivananju, B. N., Suri, A., Asokan, S. & Misra, A. Monitoring of ultraviolet pulse rate dependent photomechanical actuation in carbon nanotubes using fiber Bragg gratings. *Appl. Phys. Lett.* **104**, 013104 (2014).
- Shivananju, B. N., Asokan, S. & Misra, A. Study on effect of optical wavelength on photo induced strain sensitivity in carbon nanotubes using fiber Bragg grating. *J. Phys. D Appl. Phys.* **48**, 275502 (2015).
- Gayathri, S. et al. In situ monitoring of photostriction in chalcogenide glass film using fiber Bragg grating sensors. *Int. J. Optomechatronics* **11**, 27–35 (2017).
- Gayathri, S., Sridevi, S., Singh, G., Shivananju, B. N. & Asokan, S. Investigation of fast and sizeable photostriction effect in tellurium thin films using fiber Bragg grating sensors. *Sens. Actuators A Phys.* **279**, 688–693 (2018).
- Shivananju, B. N. et al. Graphene heterostructure integrated optical fiber Bragg grating for light motion tracking and ultrabroadband photodetection from 400 nm to 10.768 μm. *Adv. Funct. Mater.* **29**, 1807274 (2019).
- Rohatgi-Mukherjee, K. *Fundamentals of Photochemistry* (New Age International, 1978).
- Cui, X. et al. Photothermal nanomaterials: a powerful light-to-heat converter. *Chem. Rev.* **123**, 6891–6952 (2023).
- Zhang, M. et al. Recent advances on nanomaterials-based photothermal sensing systems. *Trends Anal. Chem.* **177**, 117801 (2024).
- Baffou, G., Bordacchini, I., Baldi, A. & Quidant, R. Simple experimental procedures to distinguish photothermal from hot-carrier processes in plasmonics. *Light Sci. Appl.* **9**, 108 (2020).
- Yuan, M., Wang, Y., Hwang, D. & Longtin, J. P. Thermocouple-tip-exposing temperature assessment technique for evaluating photothermal conversion efficiency of plasmonic nanoparticles at low laser power density. *Rev. Sci. Instrum.* **90**, 094902 (2019).
- Zhang, Q. et al. Characterizations for the photothermal effect of Rhodamine 6G using white-light interferometry and windowed Fourier transform. *Opt. Express* **31**, 864–876 (2023).
- Zhu, H., Gablech, E., Gablech, I. & Neuzil, P. The collective photothermal effect of silver nanoparticles probed by a microbolometer. *Commun. Mater.* **5**, 66 (2024).
- Quintanilla, M. & Liz-Marzán, L. M. Guiding rules for selecting a nanothermometer. *Nano Today* **19**, 126–145 (2018).
- Jaque, D. & Vetrone, F. Luminescence nanothermometry. *Nanoscale* **4**, 4301–4326 (2012).
- Jauffred, L., Samadi, A., Klingberg, H., Bendix, P. M. & Oddershede, L. B. Plasmonic heating of nanostructures. *Chem. Rev.* **119**, 8087–8130 (2019).
- Majumdar, A. Scanning thermal microscopy. *Annu. Rev. Mater. Res.* **29**, 505–585 (1999).
- Desiatov, B., Goykhman, I. & Levy, U. Direct temperature mapping of nanoscale plasmonic devices. *Nano Lett.* **14**, 648–652 (2014).
- Grajower, M. et al. Direct observation of optical near field in nanophotonics devices at the nanoscale using scanning thermal microscopy. *Opt. Express* **23**, 27763–27775 (2015).
- Katzenmeyer, A. M. et al. Mid-infrared spectroscopy beyond the diffraction limit via direct measurement of the photothermal effect. *Nanoscale* **7**, 17637–17641 (2015).
- Zhou, J., Smirnov, A., Dietler, G. & Sekatskii, S. K. Gap-plasmon-enhanced high-spatial-resolution imaging by photothermal-induced resonance in the visible range. *Nano Lett.* **19**, 8278–8286 (2019).
- Baffou, G. et al. Thermal imaging of nanostructures by quantitative optical phase analysis. *ACS Nano* **6**, 2452–2458 (2012).
- Bell, A. P. et al. Quantitative study of the photothermal properties of metallic nanowire networks. *ACS Nano* **9**, 5551–5558 (2015).

30. Zograf, G. P. et al. Resonant nonplasmonic nanoparticles for efficient temperature-feedback optical heating. *Nano Lett.* **17**, 2945–2952 (2017).
31. Baffou, G. Anti-Stokes thermometry in nanoplasmonics. *ACS Nano* **15**, 5785–5792 (2021).
32. Li, P. et al. Nanoscale thermometry of plasmonic structures via Raman shifts in copper phthalocyanine. *J. Phys. Chem. C* **127**, 9690–9698 (2023).
33. Proskurnin, M. A. Photothermal spectroscopy in *Laser Spectroscopy for Sensing*, 313–361 (Elsevier, 2014).
34. Proskurnin, M. A. & Kononets, M. Y. Modern analytical thermo-optical spectroscopy. *Russ. Chem. Rev.* **73**, 1143–1172 (2004).
35. Welsch, E. & Ristau, D. Photothermal measurements on optical thin films. *Appl. Opt.* **34**, 7239–7253 (1995).
36. Jacinto, C., Lima, S. M. & Catunda, T. Determination of fluorescence quantum efficiency in solutions by thermal lens measurements at several wavelengths: application to Rhodamine 6G. *J. Phys. IV Fr.* **125**, 225–227 (2005).
37. Strauss, E., Prekel, H., Otteken, D. & Reisfeld, R. Photothermal spectroscopy of Rhodamine 6G dye in organic and inorganic amorphous films in *Photoacoustic and Photothermal Phenomena II* (eds Murphy, J. C. et al.) 117–119 (Springer, 1990).
38. Bindhu, C. V. & Harilal, S. S. Effect of the excitation source on the quantum-yield measurements of Rhodamine B laser dye studied using thermal-lens technique. *Anal. Sci.* **17**, 141–144 (2001).
39. Bindhu, C. V. et al. Measurement of the absolute fluorescence quantum yield of rhodamine B solution using a dual-beam thermal lens technique. *J. Phys. D Appl. Phys.* **29**, 1074 (1996).
40. Vetrone, F. et al. Temperature sensing using fluorescent nanothermometers. *ACS Nano* **4**, 3254–3258 (2010).
41. Zhu, X. et al. Temperature-feedback upconversion nanocomposite for accurate photothermal therapy at facile temperature. *Nat. Commun.* **7**, 10437 (2016).
42. Tzeng, Y.-K. et al. Time-resolved luminescence nanothermometry with nitrogen-vacancy centers in nanodiamonds. *Nano Lett.* **15**, 3945–3952 (2015).
43. Neumann, P. et al. High-precision nanoscale temperature sensing using single defects in diamond. *Nano Lett.* **13**, 2738–2742 (2013).
44. Vasu, K. S. et al. Optical bio-sensing devices based on etched fiber Bragg gratings coated with carbon nanotubes and graphene oxide along with a specific dendrimer. *Sens. Actuators B Chem.* **195**, 150–155 (2014).
45. Hau, W. L. W., Trau, D. W., Sucher, N. J., Wong, M. & Zohar, Y. Surface-chemistry technology for microfluidics. *J. Microeng. Microeng.* **13**, 272–278 (2003).
46. Hibino, Y., Hanafusa, H., Ema, K. & Hyodo, S. Raman study on silica optical fibers subjected to high tensile stress. *Appl. Phys. Lett.* **47**, 812–814 (1985).
47. Ming, L. et al. Fabrication, characterization, and high temperature surface enhanced Raman spectroscopic performance of SiO<sub>2</sub> coated silver particles. *Nanoscale* **10**, 5449–5456 (2018).
48. Chen, S., Li, X., Guo, Y. & Qi, J. A Ag-molecularly imprinted polymer composite for efficient surface-enhanced Raman scattering activities under a low-energy laser. *Analyst* **140**, 3239–3243 (2015).
49. Kubin, R. F. & Fletcher, A. N. Fluorescence quantum yields of some rhodamine dyes. *J. Lumin.* **27**, 455–462 (1982).
50. Qiu, S. et al. Thermochemical studies of Rhodamine B and Rhodamine 6G by modulated differential scanning calorimetry and thermogravimetric analysis. *J. Therm. Anal. Calorim.* **123**, 1611–1618 (2016).
51. Liu, Y. et al. Insight into the relationship between the photostability and molecular structure of rhodamine dyes. *Tetrahedron* **149**, 133664 (2023).
52. Liu, T., Huang, J., Ding, H., Zhan, C. & Wang, S. Molecular structure perspective on temperature-sensitive properties of rhodamine aqueous solutions. *Spectrochim. Acta A Mol. Biomol. Spectrosc.* **275**, 121166 (2022).
53. Farag, A. A. M. & Yahia, I. S. Structural, absorption and optical dispersion characteristics of rhodamine B thin films prepared by drop casting technique. *Opt. Commun.* **283**, 4310–4317 (2010).
54. Nag, A. & Goswami, D. Solvent effect on two-photon absorption and fluorescence of rhodamine dyes. *J. Photochem. Photobiol. A Chem.* **206**, 188–197 (2009).
55. Birks, J. B. Fluorescence quantum yield measurements. *J. Res. Natl. Bur. Stand. A Phys. Chem.* **80A**, 389–399 (1976).
56. Yamashita, H. et al. Photochemical properties of Rhodamine-B dye molecules included within mesoporous molecular sieves in *Studies in Surface Science and Catalysis*, Vol. 117 (eds Bonneviot, L. et al.) 551–558 (Elsevier, 1998).
57. Van der Auweraer, M., Verschuere, B. & De Schryver, F. C. Absorption and fluorescence properties of Rhodamine B derivatives forming Langmuir-Blodgett films. *Langmuir* **4**, 583–588 (1988).
58. Liang, Y., Moy, P. F., Poole, J. A. & Ponte Goncalves, A. M. Fluorescence of rhodamine B on semiconductor and insulator surfaces: dependence of the quantum yield on surface coverage. *J. Phys. Chem.* **88**, 2451–2455 (1984).
59. Kemnitz, K., Tamai, N., Yamazaki, I., Nakashima, N. & Yoshihara, K. Fluorescence decays and spectral properties of rhodamine B in submono-, mono-, and multilayer systems. *J. Phys. Chem.* **90**, 5094–5101 (1986).
60. Valeur, B. & Berberan-Santos, M. N. *Molecular Fluorescence: Principles and Applications* (Wiley, 2012).
61. Omary, M. & Patterson, H. H. Luminescence theory in *Encyclopedia of Spectroscopy and Spectrometry*, 636–653 (Academic Press, 2017).
62. Majoube, M. & Henry, M. Fourier transform Raman and infrared and surface-enhanced Raman spectra for rhodamine 6G. *Spectrochim. Acta A Mol. Spectrosc.* **47**, 1459–1466 (1991).
63. Kim, H.-K., Shin, W. & Ahn, T.-J. UV sensor based on photomechanically functional polymer-coated FBG. *IEEE Photonics Technol. Lett.* **22**, 1404–1406 (2010).
64. Lakowicz, J. R. (ed.). Instrumentation for fluorescence spectroscopy in *Principles of Fluorescence Spectroscopy*, 27–61 (Springer, 2006).
65. Gan, X. et al. Graphene-controlled fiber Bragg grating and enabled optical bistability. *Opt. Lett.* **41**, 603–606 (2016).
66. Beaumont, P. C., Johnson, D. G. & Parsons, B. J. Photophysical properties of laser dyes: picosecond laser flash photolysis studies of Rhodamine 6G, Rhodamine B and Rhodamine 101. *J. Chem. Soc. Faraday Trans.* **89**, 4185–4191 (1993).

## Acknowledgements

Dr. Shivananju B.N. acknowledges financial support from the Ministry of Human Resource and Development (Sanction No. 11/9/2019-U.3(A))—Center of Excellence in Biochemical Sensing and Imaging Technologies (CenBioSIm), Ministry of Education (Sanction Number: IOE Phase II projects)—Institute of Excellence in Healthcare and Assistive Technologies, Indian Institute of Technology Madras, Science and Engineering Research Board (SERB) (Sanction No. SRG/2022/001874, EEQ/2023/000993). The authors would like to thank Bio-Sophisticated Analytical Instrumentation Facility (BIO-SAIF), Indian Institute of Technology Madras, for assistance with IX83 fluorescence microscope, Common Instruments Facility (IC&SR), Indian Institute of Technology Madras, for assistance with AFM, SEM and EDX, Sophisticated Analytical Instrumentation Facility (SAIF), Indian Institute of Technology Madras, for assistance with UV-Vis and Fluorescence spectroscopy, and RAMAN PL Facility, Department of Physics, Indian Institute of Technology Madras, for Raman spectroscopy analysis.

## Author contributions

S.B.N. conceived the idea, supervised the experiments, and acquired the funding. S.R. and S.S.S.D.K. carried out the experiments. S.R. performed additional experiments and wrote the revised manuscript with input from

S.B.N. All authors contributed to the preparation of the manuscript and approved the final version.

### Competing interests

The authors declare no competing interests.

### Additional information

**Supplementary information** The online version contains supplementary material available at <https://doi.org/10.1038/s42004-025-01880-w>.

**Correspondence** and requests for materials should be addressed to Shivananju Bannur Nanjunda.

**Peer review information** *Communications Chemistry* thanks Yang Ran and the other anonymous reviewer(s) for their contribution to the peer review of this work. A peer review file is available.

**Reprints and permissions information** is available at <http://www.nature.com/reprints>

**Publisher's note** Springer Nature remains neutral with regard to jurisdictional claims in published maps and institutional affiliations.

**Open Access** This article is licensed under a Creative Commons Attribution-NonCommercial-NoDerivatives 4.0 International License, which permits any non-commercial use, sharing, distribution and reproduction in any medium or format, as long as you give appropriate credit to the original author(s) and the source, provide a link to the Creative Commons licence, and indicate if you modified the licensed material. You do not have permission under this licence to share adapted material derived from this article or parts of it. The images or other third party material in this article are included in the article's Creative Commons licence, unless indicated otherwise in a credit line to the material. If material is not included in the article's Creative Commons licence and your intended use is not permitted by statutory regulation or exceeds the permitted use, you will need to obtain permission directly from the copyright holder. To view a copy of this licence, visit <http://creativecommons.org/licenses/by-nc-nd/4.0/>.

© The Author(s) 2026